Proceedings of the Institution of Mechanical Engineers, Part G: Journal of Aerospace Engineering

Robust multi-fidelity design of a micro re-entry unmanned space vehicle

E Minisci, M Vasile and H Liqiang

The online version of this article can be found at:

Published by:

$SAGE

On behalf of:

**Institution of
MECHANICAL
ENGINEERS**

Institution of Mechanical Engineers

**Additional services and information for *Proceedings of the Institution of Mechanical Engineers, Part G: Journal of Aerospace Engineering*
can be found at:**

Email Alerts: http://pig.sagepub.com/cgi/alerts

Subscriptions: http://pig.sagepub.com/subscriptions

Reprints: http://www.sagepub.com/journalsReprints.nav

Permissions: http://www.sagepub.com/journalsPermissions.nav

Citations: http://pig.sagepub.com/content/225/11/1195.refs.html

>> Version of Record - Nov 16, 2011

OnlineFirst Version of Record - Aug 15, 2011

What is This?

Robust multi-fidelity design of a micro re-entry unmanned space vehicle

E Minisci[1], **M Vasile**[2]*, and **H Liqiang**[3]

[1]School of Engineering, University of Glasgow, Glasgow, UK
[2]Department of Mechanical Engineering, University of Strathclyde, Glasgow, UK
[3]State Key Laboratory of Astronautic Dynamics, Xi'an Satellite Control Center, Shaanxi, People's Republic of China

Abstract: This article addresses the preliminary robust design of a small-scale re-entry unmanned space vehicle by means of a hybrid optimization technique. The approach, developed in this article, closely couples an evolutionary multi-objective algorithm with a direct transcription method for optimal control problems. The evolutionary part handles the shape parameters of the vehicle and the uncertain objective functions, while the direct transcription method generates an optimal control profile for the re-entry trajectory. Uncertainties on the aerodynamic forces and characteristics of the thermal protection material are incorporated into the vehicle model, and a Monte-Carlo sampling procedure is used to compute relevant statistical characteristics of the maximum heat flux and internal temperature. Then, the hybrid algorithm searches for geometries that minimize the mean value of the maximum heat flux, the mean value of the maximum internal temperature, and the weighted sum of their variance: the evolutionary part handles the shape parameters of the vehicle and the uncertain functions, while the direct transcription method generates the optimal control profile for the re-entry trajectory of each individual of the population. During the optimization process, artificial neural networks are utilized to approximate the aerodynamic forces required by the optimal control solver. The artificial neural networks are trained and updated by means of a multi-fidelity approach: initially a low-fidelity analytical model, fitted on a waverider type of vehicle, is used to train the neural networks, and through the evolution a mix of analytical and computational fluid dynamic, high-fidelity computations are used to update it. The data obtained by the high-fidelity model progressively become the main source of updates for the neural networks till, near the end of the optimization process, the influence of the data obtained by the analytical model is practically nullified. On the basis of preliminary results, the adopted technique is able to predict achievable performance of the small spacecraft and the requirements in terms of thermal protection materials.

Keywords: multi-objective evolutionary algorithms, robust multi-disciplinary design, meta-modelling, optimal control, unmanned space vehicles

1 INTRODUCTION

Owing to the increasing capabilities of modern computers, numerical simulation has been substituting a big portion of experimental tests, and numerical optimization allows handling complex multidisciplinary

Corresponding author: Department of Mechanical Engineering, University of Strathclyde, 75 Montrose Street, Glasgow G1 1XJ, UK.

email: massimiliano.vasile@strath.ac.uk

design problems. The optimization of engineering systems means lower costs and better performance but requires considerable computing resources. Up to now, on sequential machines, reduced or low-fidelity models have been generally used during the optimization process and higher fidelity models have been used only for deeper investigation of some obtained optimal configurations. Nowadays, newest parallel/distributed resources, such as Beowulf clusters and grids, allow different and more efficient approaches, where the high-fidelity models can be directly used during the optimization phase. However, since computational resources are never available in the ideal infinite amount, low to medium, and high-fidelity models can be used during the optimization process, to limit the request for computational resources to a predefined level: low-fidelity models are used for the preliminary space exploration and high-fidelity ones towards the end of the process, when the search is focused in a more limited area [1–4].

This article presents the robust design optimization of a small-scale unmanned space vehicle (USV), by means of an incremental single process (ISP) approach, which implements a multi-fidelity strategy and allows for dealing with the complexity and computational costs of the multidisciplinary optimization process. The ISP consists of a single, integrated optimization, in which the initial iterations are performed with a low-fidelity model, and the complexity and fidelity of the model are progressively increased during the optimization process. An additional level of difficulty is introduced by the fact that the USV operates through different flow regimes, from hypersonic, in upper atmosphere, to supersonic and subsonic, as it approaches the Earth surface. For this reason, the fidelity of the aerodynamic model must be differently managed, depending on the regime.

A meta-modelling technique, based on artificial neural network (ANN) approximators, is used to reduce the cost of aerodynamic computations. During the optimization process, the aerodynamic database used to generate the meta-model is updated with the outcomes of models with different fidelities [5, 6]. In particular, low-fidelity ones will be used to generate samples globally over the range of the design parameters, while high-fidelity models will be used to refine the meta-model locally, in later stages of the optimization.

The optimization process is based on an evolutionary algorithm combining global and local search. At every step of the evolutionary algorithm, an optimal control problem, associated to each individual of the population, is solved with a direct transcription method. Two direct transcription methods were tested: finite elements in time defined on spectral basis [7, 8] and Gauss pseudospectral methods [9]. Both methods are similar in nature and perform similarly on this problem.

Unmanned space vehicles are seen as a test-bed for enabling technologies and as a carrier to deliver and return experiments to and from low-Earth orbit. USVs are a potentially interesting solution also for the exploration of other planets or as long-range recognisance vehicles. As test bed, USVs are seen as a stepping stone for the development of future generation re-usable launchers but also as way to test key technologies for re-entry operations.

Examples of recent developments are the PRORA-USV [10–12], designed by the Italian Aerospace Research Center (CIRA) in collaboration with Gavazzi Space, or the Boeing X-37B Orbital Test Vehicle (OTV), that is foreseen as an alternative to the space shuttle to deliver experiments into Earth orbit. Among the technologies to be demonstrated with the X-37 are improved thermal protection systems, avionics, the autonomous guidance system, and an advanced airframe.

Here, following the path that brought from satellites to current micro-cube satellites, the first approach to the design of a small-scale USV is described. The goal of the project is to derive the technical specifications for a small and relatively inexpensive vehicle which could be used as a technological demonstrator. The design is carried out taking into account the availability of last generation thermal protection systems (TPS) based on ultra-high temperature ceramic materials (UHTC), which are currently considered for the design of the PRORA vehicle [13, 14]. UHTC is a family of ceramic materials with extremely high melting temperatures, good oxidation resistance in reentry-type environments, and reasonably good thermal shock resistance, which can be used to protect small radius edges of the new generation high efficiency spacecrafts.

For this study, the parameterized shape is based on an ideal waverider configuration [15–17], but the geometry of the ideal waverider is here modified in order to introduce more realistic rounded edges.

Some of the parameters defining the shape of the vehicle plus the thickness of the TPS at the nose are considered as the unknowns of the external evolutionary process, aimed at searching for vehicles that can re-enter with the smallest heating stresses. The performance of each individual of the population depends on the results of a trajectory optimization problem, where the angle of attack as function of time, $\alpha(t)$, is optimized to minimize the maximum value of the heat flux (Fig. 1). Some properties of the vehicle, like those of the TPS material and the
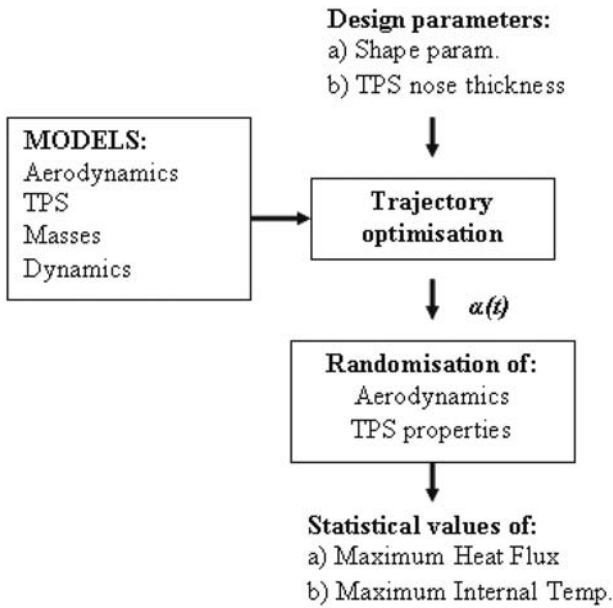
Fig. 1 Description of the internal loop process

aerodynamic approximated model, are randomized and mean and variance of the maximum heat flux and maximum internal temperature are computed and utilized as objective and constraint functions for the external optimization loop. The trajectory optimization requires the definition of vehicle models such as the aerodynamic, thermal, structural, and dynamic (the vehicle is considered as a material point) ones.

This article starts by describing the models of the vehicle, and then details the robust multidisciplinary design approach based on ISP, together with the modelling and treatment of model uncertainties. Some preliminary results show the achievable performance of this type of vehicle and a trade-off between optimality and robustness.

2 USV SYSTEM MODELS

This section introduces all system models used to compute the characteristics of the vehicle: geometry,

aerodynamic forces, heat flux, dynamics, and kinematics.

2.1 Geometry and shape model

The vehicle is a modified version of a waverider with rounded edges. The waverider baseline geometry is defined by three two-dimensional (2D) power-law equations [17]. The planform and the upper surfaces of the vehicle are parameterized by the length l, the width, w, a power law exponent n, the vehicle centre line wedge angle, θ, and β, which is the oblique shock wave inclination angle [17]. An example can be found in Fig. 2, where the original waverider sharp-edge shape is modified to introduce a rounded edge with radius of curvature, $R_n > 0$. For the example in Fig. 2, the parameters defining the shape are: $l = 1.0$ m, $w = 0.8$ m, $n = 0.3$, $\theta = 10°$, $\beta = 12°$, $R_n = 0.02$ m. In this study, l, w, n, θ, and R_n will be considered unknowns of the shape optimization problem, while β will be considered constant.

2.2 Aerodynamic models

Two different models are used to predict the aerodynamic characteristics of the vehicle. The former one is a simplified analytical model, which is here applied to the actual rounded-edge vehicle, although it was originally developed to predict the aerodynamics of the original sharp-edge shape of the waverider configuration [17], in order to have a very first approximation of the performance at the early stage of the design process. The latter one is a full high-fidelity computational fluid dynamic (CFD) model based on a finite volume integration of Reynolds-averaged Navier–Stokes equations (RANS).

2.2.1 Analytic hypersonic model

The analytic model gives the lift L and wave drag D_w as functions of the pressure on the upper, lower, and base surfaces [17], which can be calculated
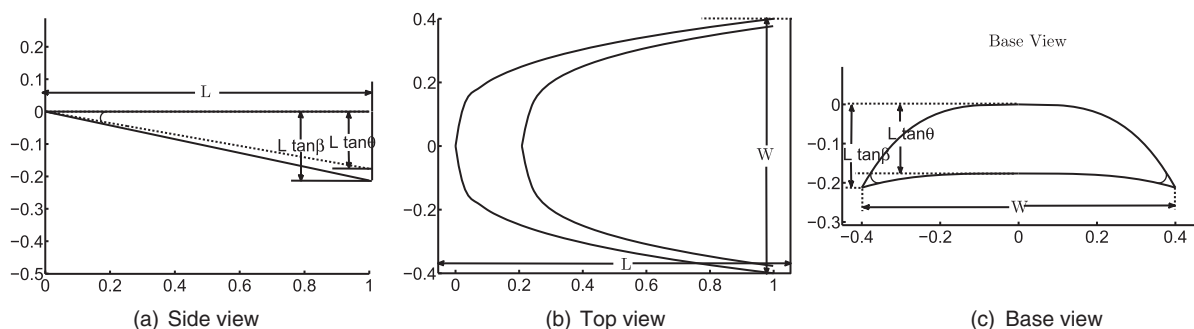
Fig. 2 Example of vehicle geometry: $l = 1.0$ m, $w = 0.8$ m, $n = 0.3$, $\theta = 10°$, $\beta = 12°$, $R_n = 0.02$ m

analytically with the oblique shock theory or Prandtl–Meyer expansion theory [18], while the viscous drag D_v is given in analytical form, using the reference temperature method [19].

The total drag D is $= D_w + D_{v,u} + D_{v,b}$, where $D_{v,u}$ and $D_{v,l}$ are the viscous drags of the upper and lower surfaces, respectively.

As previously anticipated, this simplified model still considers the sharped shape of the wave rider, and does not take into account the introduction of the rounded edges.

2.2.2 CFD model

A commercial code (*Numeca®*), solving the RANS equations, is used to obtain high-fidelity solutions almost in the entire flight envelope and also to compute initial solutions when the analytical model cannot be applied (for super- and sub-sonic flight regimes).

The computational domain is discretized by a multi-block structured mesh made by 13 blocks with near $1.2 \ 10^6$ total nodes. For each configuration, the mesh is changed and adapted to the current geometry by internal scripting on the basis of design parameters. Since no out-of-plane flight conditions are considered, only half of the actual domain is discretized and mirror plane conditions are imposed into the longitudinal plane.

Four different settings are implemented and used during the process:

(a) laminar hypersonic for Mach number, Ma, > 6.25 and Reynolds number, Re, $< 9.5 \ 10^4$;
(b) fully turbulent (no transition model is considered) hypersonic for $Ma > 6.25$ and $Re > 1.05 \ 10^5$;
(c) laminar supersonic and subsonic for $Ma < 5.75$ and $Re < 9.5 \ 10^4$;
(d) fully turbulent supersonic and subsonic for $Ma < 5.75$ and $Re > 1.05 \ 10^5$.

For hypersonic conditions, the radiative equilibrium temperature at the nose is imposed on the solid boundaries. Real gases database is enhanced on the basis of reported air data for high temperatures [20]. Since non-equilibrium reactions and ionization are not taken into account, it should be expected to obtain underestimation of the drag at the highest altitudes, with a consequent underestimation of the deceleration during the first part of the re-entry, while this simplification should not affect the lift values [21].

No solutions are computed for $5.75 \leqslant Ma \leqslant 6.25$ or $9.5 \ 10^4 \leqslant Re \leqslant 1.05 \ 10^5$, in order to have an aerodynamic database as smooth as possible: since there is no transition model between laminar and turbulent flow and there is discontinuity between the models for hypersonic and supersonic regimes, then computations into the transition regions could be misleading. The aerodynamic characteristics will be approximated by a smooth ANN system, then the ANN itself will provide smooth approximations of the characteristics in the transition regions.

2.3 TPS and thermal model

The thermal protection system (TPS) is assumed to be made of zirconium diboride (ZrB_2) UHTC, which has thermal properties, as given in Table 1 [22].

At this point of the project, the authors bound the angle of attack to a maximum value of $20°$; hence, the highest heat flux is expected to be at the USV nose cap. Thus, the whole nose cone is made of UHTC with thickness L_{TPS}, which will be considered as design parameter. The rest of the vehicle is covered with a thin shell with a constant thickness of 0.003 m [22].

For the design process, the convective heat flux is computed in the simplest way with the analytical formula [23]

$$\dot{q}_{conv} = K_e \sqrt{\frac{\rho_\infty}{R_n}} V_\infty^3 \qquad (1)$$

where $K_e = 1.742 \ 10^{-4}$ (for the heat flux $\dot{q}_{conv}$ in W/m^2).

The internal temperature (T_{int}) is computed by solving the following 1D heat equation at the nose cap

$$\frac{\partial^2 T}{\partial x^2} = \frac{c \ \rho_{TPS}}{k} \frac{\partial T}{\partial t} \qquad (2)$$

with boundary conditions

$$\dot{q}_{conv} - \epsilon \ \sigma \ T_w^4 + k \frac{dT}{dx} \quad \text{at} \quad x = 0$$
$$k \frac{dT}{dx} = \epsilon \ \sigma \ T_{int}^4 \quad x = L_{TPS} \qquad (3)$$

where c is the heat capacity, ρ_{TPS} the density of the TPS material, k the thermal conductivity, ϵ the material emissivity, and σ the Stephen–Boltzmann's constant [24]. Note that neither dissipation nor radiation through the structure is considered, and only radiation on the back of the nose cap vehicle is taken in account. As a consequence of this, the authors expect that the internal temperature is overestimated, and that a re-entry trajectory with a short arc with high $\dot{q}_{conv}$ might have an internal temperature,

Table 1 ZrB_2 properties

Properties		unit
Density	6000	kg/m^3
Specific heat	628	J Kg^{-1} K^{-1}
Thermal conductivity	66	W m^{-1} K^{-1}
Emissivity	0.8	

which is lower than a trajectory with a long arc with lower heat flux.

2.4 Mass model

The total mass of the USV is made of the structural mass m_{st}, the mass of the TPS m_{TPS}, and the mass of the payload (avionics and power system) m_{pl}

$$m = m_{TPS} + m_{st} + m_{pl} \tag{4}$$

The mass of the payload is here assumed to be about 20 per cent of the structural mass; therefore, $m_{pl} = 0.2$ m_{st}. The mass of the TPS is made of the mass of the nose $m_{nose} = \rho_{TPS} V_n$ plus the mass of the thin skin covering the rest of the vehicle m_{skin}, where V_n is the volume of the nose and ρ_{TPS} the density of the TPS material. The mass of the TPS skin covering the vehicle, except the nose, is

$$m_{skin} = \rho_{TPS} S_{TPS} d_{TPS} \tag{5}$$

where d_{TPS} is the thickness of the TPS, and S_{TPS} the surface area except that of the nose, which can be approximated by $S_{TPS} = 2S_{pE} + S_{bE} - S_n$ (S_{pE} and S_{bE} are the total planform surface and the area of the rear part of the rounded edge waverider, respectively, and S_n the surface of the TPS nose).

The structure of the vehicle is supposed to be made of titanium, with a density of $4400 \, kg/m^3$. The structural mass m_{st} can be obtained from

$$m_{st} = \rho_{body}(2S_{pE} + S_{bE})d_{boby} \tag{6}$$

where in this case, $d_{boby} = 0.004 \, m$ is the thickness of the structure of the vehicle, seen as a shell.

2.5 Dynamic equations and optimal control subproblem

The vehicle is considered to be a point mass, whose motion is governed by the following set of dynamic equations [25]

$$\begin{cases} \dot{r} = v sin\theta_p \\ \dot{\lambda} = \dfrac{v cos\theta_p cos\xi}{r cos\phi} \\ \dot{\phi} = \dfrac{v cos\theta_p sin\xi}{r} \\ \dot{v} = -\dfrac{D(\alpha)}{m} - g sin\theta_p \\ \dot{\theta}_p = \dfrac{L(\alpha)}{mv} cos\gamma_v - \left(\dfrac{g}{v} - \dfrac{v}{r}\right) cos\theta_p \\ \dot{\xi} = \dfrac{L(\alpha)}{mvcos\theta} sin\gamma_v - \dfrac{v}{r} cos\theta_p cos\xi tan\phi \end{cases} \tag{7}$$

where r is the norm of the position vector with respect to the centre of the planet, λ the longitude, ϕ the latitude, v the magnitude of the velocity, θ_p the flight

path angle, and ξ the heading angle (azimuth of the velocity). No out-of-plane manoeuvres are considered; thus, γ_v is kept equal to zero during the whole trajectory. The angle of attack α is the control variable; therefore, for each geometry the following optimal control subproblem needs to be solved

$$\min_{\alpha} \max_{t} \dot{q} \tag{8}$$

subject to dynamic equations (7) and terminal conditions

$$\begin{cases} r(t = 0) = r_0 \\ \lambda(t = 0) = \lambda_0 \\ \phi(t = 0) = \phi_0 \\ v(t = 0) = v_0 \\ \theta_p(t = 0) = \theta_0 \\ \xi(t = 0) = \xi_0 \\ r(t = t_f) \leqslant r_f \\ r(t = t_f) \geqslant r_{min} \end{cases} \tag{9}$$

The re-entry time is free and no other terminal conditions are imposed as there is no specific requirement on the landing point. Note that thermal equation (2) is solved only once an optimal trajectory is obtained from the solution of problem (8). In fact, every optimal control profile is re-propagated forward in time and heat flux and internal temperature are computed with equations (1) and (2).

3 ROBUST MULTIDISCIPLINARY DESIGN APPROACH

The design of the micro-USV requires the simultaneous optimization of the shape and trajectory control profile of the vehicle. In fact, both of them have an impact on the maximum heat flux that the vehicle has to withstand and therefore on its mass, size, and shape.

The approach taken in this article hybridizes an evolutionary multi-objective algorithm with a direct transcription method for optimal control problems. The evolutionary part handles the shape parameters and the global optimization of the performance indexes, i.e. mean values of heat flux and thermal load, and their variances. The performance indexes of each individual in the population are the results of the optimal control profile coming from the solution of a non-linear programming problem. The trajectory optimization part of the algorithm relies on an artificial neural network system, which approximates the aerodynamic forces acting on the vehicle (two distinct ANNs are used to approximate the lift and the drag). The aerodynamic forces are a function of the shape of the vehicle and its operation

conditions, such as the angle of attack, α, the speed, v, and the altitude H (defined $H = r - R_E$, where R_E is the mean radius of the Earth). In order to reduce the computational costs related to the training and updating of the ANNs, a multi-fidelity incremental approach is adopted.

3.1 Robust design optimization under uncertainty

The USV is designed to follow a re-entry trajectory that minimizes the heat flux. A second performance index is the internal temperature that together with the heat flux defines the mass of the TPS.

Optimal control problem (8) considers the deterministic value of the maximum heat flux coming from an optimal α profile. However, a number of model elements can be considered uncertain, such as the aerodynamic forces and the characteristics of the thermal protection material.

Therefore, one can associate to the nominal value of lift L_{det} and drag D_{det}, the uncertain quantities

$$
\begin{aligned}
L_{unc} &= L_{det} + Err(\alpha, v, H)C_E(\alpha, v, H)L_{det} \\
D_{unc} &= D_{det} + Err(\alpha, v, H)C_E(\alpha, v, H)D_{det}
\end{aligned}
\tag{10}
$$

where Err is an error function, which depends on the angle of attack, the speed, and the altitude H; and C_E is a parametrical sampling hyper-surface, which maps a triplet of values of angles of attack, speed, and altitude into the interval $[-1, 1]$. Since the idea is that the uncertainties of the aerodynamic data increase with the angle of attack, speed, and altitude; then, Err is modelled here as a linear three-dimensional (3D) surface, with values that vary from 0.2, when angle of attack, speed, and altitude are $= 0$, to 0.8, when the incidence is $= 20°$, the speed is $= 8000\,\mathrm{m/s}$ and the altitude is $100\,\mathrm{km}$. Some of the characteristics of the thermal protection material are considered uncertain as well. In particular, the thermal conductivity, k, and the specific heat, c, can uniformly vary in the range ± 0.1 of the reference value.

Thus, given a nominal trajectory with an optimal control profile α^*, N_s trajectories are re-propagated. For each one of the N_s trajectories, a different C_E surface is built on the basis of sampled random parameters, in order to obtain the uncertain values for L, D for the entire flight envelope. New values of k and c are sampled in the neighbourhood of the deterministic value, as well. Then, the mean, E_q and E_T, and the variance, σ_q^2 and σ_T^2, are computed on the basis of the results of the randomized re-propagation and eventually used as performance indexes for the external loop, which optimizes the shape.

Based on this definition of the performance indexes, the robust design optimization under uncertainties can be formulated as follows

$$
\min_{d \in D}[E_q, E_T, \sigma_q^2 + \sigma_T^2]
\tag{11}
$$

subject to the following constraints on the variance

$$
\sigma_q^2 \leqslant \bar{\sigma_q^2}; \; \sigma_T^2 \leqslant \bar{\sigma_T^2}
\tag{12}
$$

the design vector $\boldsymbol{d}$ is defined as follows: $\boldsymbol{d} = [l, w, n, \theta, R_n, L_{TPS}]$ (five shape parameters plus the parameter defining the dimension of the nose cone TPS structure).

Note that a precise model of the uncertainties should also consider other factors, such as: (a) the fidelity of the model (analytical vs. CFD), (b) the quality of the solution (e.g. relative quality of the mesh for CFD calculations, convergence level of the CFD runs and the NLP problem), and (c) meta-modelling approximation error introduced by the ANNs. All these aspects are under current investigation and will be presented in future works. Previous points (a) and (b) will require a mesh sensitivity analysis and an extensive computation campaign to assess the errors introduced by approximations at different levels of fidelity. While point (c) can be accomplished by integrating a term, which is related to the density of available verified solutions, in the Err function. In this respect, the point (c) is the easiest to handle, but also the least important one: since the ANNs are updated by an evolution control approach, then the related uncertainty is also reduced during the process and almost nullified in the optimal region.

3.2 Multi-objective algorithm

The multi-objective optimization (MOO) problem (11) was solved with a particular type of evolutionary algorithm which belongs to the sub-class of estimation of distribution algorithms (EDAs) [26]. EDAs derive from one of the ways researchers tried to overcome difficulties in finding good solutions for complex problem by simpler evolutionary, genetic algorithms. Generally, these methods, starting from the current population, build a probabilistic model of the search space, then explore the search space by a sampling procedure that operates on the probabilistic model, replacing the usual cross-over and mutation operators. EDAs ensure an effective mixing and reproduction of solution substructures due to their ability to accurately capture the structure of the given problem.

The specific EDA employed in this study is derived from the MOPED (multi-objective parzen based estimation of distribution) algorithm [27, 28]. MOPED is

a multi-objective optimization algorithm for continuous problems that uses the Parzen method to build a probabilistic representation of Pareto optimal solutions, with multivariate dependencies among variables. Non-dominated sorting and crowding operators [**29**] are used to classify promising solutions in the objective space, while new individuals are obtained by sampling from the Parzen model.

The Parzen method [**30**] is a non-parametric approach to kernel density estimation, which gives rise to an estimator that converges everywhere to the true probability density function (PDF) in the mean square sense. Should the true PDF be uniformly continuous, the Parzen estimator can also be made uniformly consistent. In short, the method allocates exactly n_k identical kernels, each one centred on a different element of the sample. More details on the original code can be found in the cited works. In the next section, the trajectory optimization code and the evolutionary control technique with multi-fidelity are detailed.

3.2.1 Trajectory optimization

Problem (8) with constraint equations (7) and (9) was transcribed with a Gauss pseudospectral method and with finite elements in time on spectral basis [**7**]. The two approaches gave similar results; therefore, it was decided to omit from this article the comparison between the two approaches on this particular problem. In both cases, the trajectory is decomposed in N elements, each of which have n_p collocation points. After transcription, the optimal control problem defined by equations (7) to (9) becomes the following general non-linear programming problem

$$\min_{\alpha_s} \max_{t_s} \dot{q}_s \tag{13}$$

subject to the non-linear algebraic constraints

$$C(r_s, \lambda_s, v_s, \xi_s, \theta_s, \alpha_s, t_s) = 0 \tag{14}$$

and the terminal constraints

$$\begin{cases} r(t=0) = r_0 \\ \lambda(t=0) = \lambda_0 \\ \phi(t=0) = \phi_0 \\ v(t=0) = v_0 \\ \theta_p(t=0) = \theta_0 \\ \xi(t=0) = \xi_0 \\ r(t=t_f) \leqslant r_f \\ r(t=t_f) \geqslant r_{min} \end{cases} \tag{15}$$

where r_s, λ_s, ϕ_s, v_s, ξ_s, θ_s, α_s, and t_s are the discrete values of the time, states, and control values at the nodes of the transcription scheme. The NLP problem

was solved with the Matlab® function *fmincon*. Two different solution algorithms were tested: *active-set* and *interior-point*. The latter demonstrated a superior robustness and convergence speed.

3.3 Evolution control and multi-fidelity approach

The basic idea underneath evolution control (EC) approaches is to use, throughout the optimization process, both the true and the surrogated models in a way that reduces the total computational time, without loosing in precision.

Due to the necessity to limit the number of training samples, it is very difficult to construct an initial approximated model that is globally correct. Most likely, the approximation will bring the optimization algorithm to false optima, i.e. solutions that are optimal for the approximated model but are suboptimal for the true functions.

Model management or evolution control techniques address this problem and avoid finding false optima, or missing true ones.

Jin *et al.* [**31**] in their paper propose two different approaches for the evolution control of the model: (a) individual-based control and (b) generation-based control. In the first approach, n_v individuals in the current population are chosen and evaluated with the true model at each generation. In the latter, the whole population is evaluated with the real model, every n_{gcyc} generations, for n_{gv} generations, where $n_{gv} < n_{gcyc}$. The individuals evaluated with the true model are then introduced into the dataset in order to locally improve the surrogated model in the promising regions.

The method adopted for this study is a mix of both evolution control strategies. Figure 3 summarizes the whole optimization process. The MOO optimization algorithm MOPED is integrated with an external procedure that monitors the status of the approximated models. At the end of each iteration (generation), the external procedure checks if an updated version of the approximated model is ready and available. If the approximated model is updated, then all the individuals in the current population are re-evaluated and re-classified with the updated model, before the Parzen distribution is updated and sampled. If the approximated model is not updated, because, for example, a CFD computation is still running, and the difference between the generation of the previous update and the current generation is n_{gcyc}, then MOPED pauses and waits for the new update.

In an asynchronous way, an additional external procedure (bottom right block in Fig. 3) manages the training and updating of the approximated model.
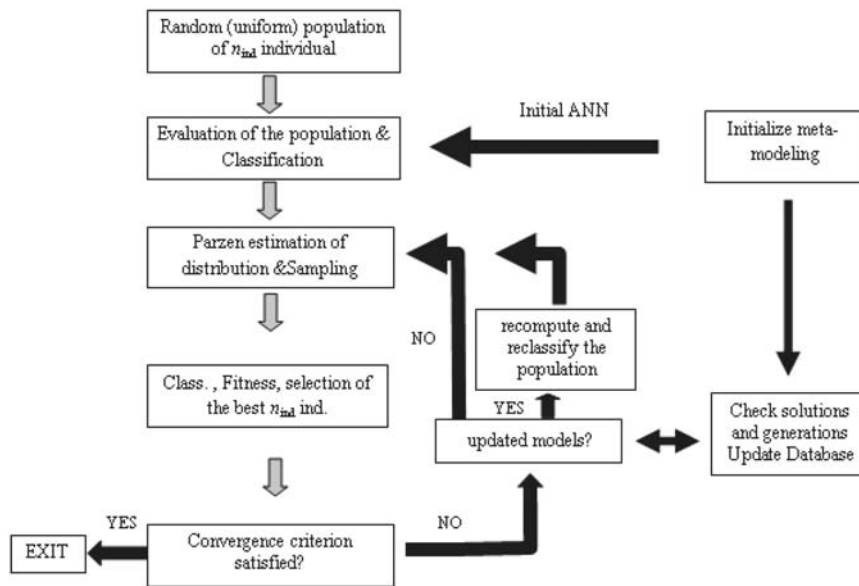
Fig. 3 MOPED with evolutionary control modification and independent approximator handler

This procedure needs as input a list of system models ordered by increasing level of fidelity and a scheduling report detailing how and when the different models should be used. Then, it extracts for each optimal trajectory the matrix $\mathbf{S}_{opt} = [l, w, n, \theta, R_n, \alpha, \mathbf{v}, \mathbf{H}]$. Each row in matrix $\mathbf{S}$ corresponds to a point along the trajectory. Each row in $\mathbf{S}$ is then compared to the values in $\mathbf{DB}_{train1}$, the matrix of points in the database used to train the ANNs. The procedure works as follows.

1. At generation 0, it trains a first ANN system using the low-fidelity model (fidelity level 0) and then passes the ANNs to MOPED (process *Initialize App 0* in Fig. 3); $\mathbf{DB}_{train}$ is initialized.
2. At each subsequent generation:
   (a) Initialize counter $i_c = 0$;
   (b) while $i_c <= n_t$
      (i) extract from the population a sampled trajectory and extract n_o operative points;
      (ii) for i $= 1 \ldots n_o$
         – compute the minimum Euclidean distance $d_{sl,i} = min_j |S_{opt,i} - DB_{train,j}|$ where j loops over all the points in the database (the rows of DB_{train});
         – if $d_{sl,i} > d_{min,sl}$, then the point $S_{opt,i}$ is evaluated and immediately inserted into the database DB_{train}, and $i_c = i_c + 1$; all the solutions in the database that were computed with a lower fidelity model and have $d_{sl} < d_{min,ll}$ are discarded from future updates of the approximating model;

      – if $i_c = n_t$ interrupt loops.
3. Every n_{gl} generations of the global optimizer, it increases the level of fidelity of the model, till the maximum level is reached.

3.4 Surrogate model

General principles of evolution control do not depend on any specific approximation technique but, of course, the approximation approach strongly affects the outcome of any EC strategy. Due to the particular task, the approximator should be able to filter the noise of the CFD models responses and correctly generalize in the broad range of shape parameters and operative conditions. Response surfaces and artificial neural networks were considered [32–34], but ANNs have been preferred, because they are more robust and generally useful when there is no information on the general structure of the function to approximate.

When dealing with ANNs, usually radial basis NNs are preferred due to the modest computational effort required to train them [33, 34], but here the generic multi layer perceptron (MLP) ANN with one hidden layer was used, due to the expected better generalization in regions *far* for the training data, and because the computational cost and time of the online learning and update is negligible if compared to a call to the high-fidelity model. The last point is even truer in this case, because the approximator does not directly approximate the objective and/or constraint functions, but it is used to obtain a cheap aerodynamic

surrogate model of the system, which is necessary to run the optimal control solver and then is called thousands of times for each individual.

The training process is based on a Bayesian regularization back-propagation [35], which limits any overfitting problem, and whose additional costs are to be considered negligible as well.

The eight inputs to the ANN approximators are: the five geometric parameters (l, w, n, θ, and R_n), the angle of attack, the speed, and the altitude. The outputs are the coefficients of lift, C_L and drag, C_D. The networks are trained to reach a mean squared error of 1 per cent on the normalized training output.

4 OPTIMIZATION RESULTS

The design space for problem (11) is defined by the following bounds on the design parameters: the nominal length $l \in [0.9, 1.5]$[m], the nominal width $w \in [0.4, 0.9]$[m], the exponent $n \in [0.2, 0.7]$, the angle $\theta \in [6, 11,9]$[°], the radius of the nose $R_n \in [0.0115l, 0.026l]$, the thickness of the TPS at the nose $L_{TPS} \in [0.05, 0.15]$[m]. The angle β, as defined in Section 2.1, is kept fixed to 12°. Constraints are set as $\sigma_q^2 = \sigma_T^2 = 1000$.

The trajectories are discretized with five elements, each one with seven nodes. The bounds on the variables of the trajectory optimization are: total time $T_{tot} \in [500, 6500]$[s], angle of attack $\alpha \in [0, 20]$[°], radius $r \in [6.380 \ 10^6, 6.480 \ 10^6]$[m], longitude $\lambda \in [-200, 20.9559]$[°], latitude $\phi \in [-200, 68.0767]$[°], speed $v \in [20^2, 10^4]$[m/s], flight path angle $\theta_p \in [-30, 10]$[°], heading angle $\xi \in [-225.7396, -55.7396]$[°].

The initial conditions (9) are $x_0 = [R_E + 10^5, 20.9559, 68.0767, 7700, -0.63247, -145.7641]^T$, where R_E is the mean radius of the Earth, while the constraints on the final conditions are $r_f = R_E + 25000$ m and $r_{min} = R_E + 15000$ m.

The MOO process was run for 55 generations with a population of 60 individuals. The initial approximators were built with 1000 samples coming from 1000 analytic model computations. The samples were selected with a randomized Latin Hypercube. Additionally, 100 super- and subsonic CFD computations were added to the training set to allow the approximators to have an extended range of validity, without the need to extrapolate. The computation of the first database required nearly 700 h of computational time, distributed on a cluster of 15 linux 64 processors (2 days of effective time). The computations of the CFD solver were stopped when convergence was obtained on the aerodynamic forces.

The characteristic parameters of the evolution control process were set as follows: $n_t = n_o = 10$, $n_{gl} = 10$,

for a total of two switches; $n_{gcyc} = 5$; $d_{min,sl} = 0.3$ (all the inputs are normalized to $[-1, 1]$); $d_{min,ll} = 1.2$.

At level 1, which is considered from generation 10, CFD computations were used to verify the trajectory points up to 50 km. At level 2, the altitude limit for the use of CFD computation is increased to 90 km, even if the validity of the models at this altitude is at least questionable.

During the computation, until generation 50, the solutions obtained with the CFD model increased up to 465 (the results of more than 30 CFD runs were not inserted into the database, because they did not properly converge), allocated in the promising region of the search space, while the analytical ones, used to build the ANN approximators, decreased to nearly 200. From generation 50 to 55, no more new verified values are added to the ANN database.

The approximation of the Pareto front at the end of the optimization process is shown in Fig. 4. The front is sparse and irregular, but this was expected, and it is due to many different reasons: (1) the objective functions, which are the outcome of a min-max problem and of a Monte-Carlo sampling, are extremely noisy; (2) 60 individuals in the populations are not enough to properly cover the front, but the chosen number is a trade-off between exhaustiveness of the search and needed computational resources; (3) moreover, the speed and accuracy of convergence of the trajectory optimization loop is quite sensitive to shape parameters and initial conditions. Better converge and front approximation could be obtained with a better initial guess for the control law. In this study, the initial guess for every individual had the following characteristics: incidence at time $t = 0$ is 18° and is linearly decreased, with decrements $d\alpha = 1/550$[deg/sec], till the last point of the trajectory obtained by direct integration satisfies the constraints on the required final altitude.

In Fig. 5 individuals A, B, and C minimize the mean value of the maximum heat flux, the mean value of the maximum internal temperature, and the sum of the variances, respectively.

The optimization is mainly driven by the easiest way to reduce, or limit, the heat flux at the nose, i.e. increasing the radius of the nose. This is apparently due to the use of the analytical model, which overestimates the performance of the vehicle when the radius of the edges becomes considerably big. Even if the use of simplified solutions is limited toward the end of the optimization process, the analytical model biases the search path from the beginning of the process. Moreover, it is the only model used to predict performance of the solutions for altitudes higher than 90 km. However, in spite of that, the code is also able to correlate a smaller radius of curvature at the nose
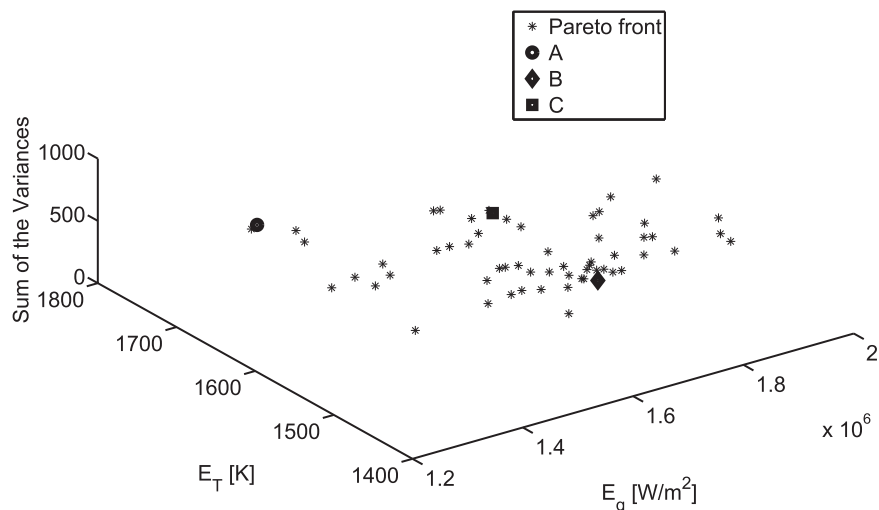
Fig. 4   Approximation of the Pareto Front at the end of the optimization process
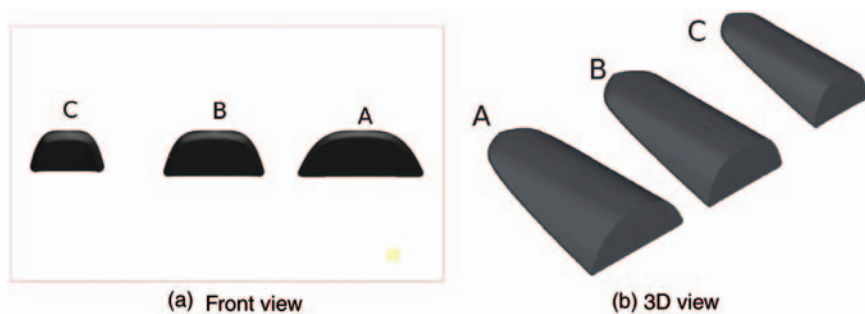
Fig. 5   Optimal solutions: individual A minimizes the mean value of the maximum heat flux,
individual B minimizes the mean value of the maximum internal temperature, while
individual C minimizes the sum of the variances

with better aerodynamic performances in hypersonic regime.

The design parameters for solutions A, B, and C are:

Solution A: $l = 1.496\,44$; $w = 0.881\,58$; $n = 0.2964$;
  $\theta = 11.9014$; $R_n = 0.026\,06$; $L_{TPS} = 0.061\,18$
Solution B: $l = 1.493\,42$; $w = 0.706\,51$; $n = 0.2291$;
  $\theta = 11.7633$; $R_n = 0.031\,93$; $L_{TPS} = 0.142\,50$
Solution C: $l = 1.380\,74$; $w = 0.526\,09$; $n = 0.2375$;
  $\theta = 11.3022$; $R_n = 0.035\,89$; $L_{TPS} = 0.093\,93$

Figure 6 shows the nominal, deterministic trajectories of the three selected individuals. Individual A, due to better aerodynamic performance, is able to follow a higher re-entry path in the critical part of the trajectory, limiting the heat loads (Fig. 7), even if it is about 20 per cent heavier than solution B, and considerably heavier than C (the masses of individuals A, B, and C are 69, 58.8, and 36.8 kg, respectively). On the other hand, solution C, which is worse in terms of mean values, is the most robust one.

The trajectory optimization process, and, as a consequence, the shape of the vehicles are strongly affected by the model of the internal temperature, which correlates the function E_T only to the parameter L_{TPS}, with smaller dependence on the trajectory path. Good performance of individual B in terms of E_T is basically due to the thick TPS cone at the nose. For the same reason, even if solution of type A can fly along a higher altitude path, because of a thinner layer of thermal protection material at the nose, it has higher internal temperatures.

As expected, the vehicles pass through the critical part of the atmosphere with an angle of attack which is close or equal to the upper limit (Fig. 8). For such an incidence, the stagnation point is still on the nose (as can be seen from Fig. 9), but for a real application, it is likely that blunt-body shapes similar to the ones obtained in this study, would even require a higher value of the angle of attack, around 40–45°. In this case, the stagnation point might move towards the
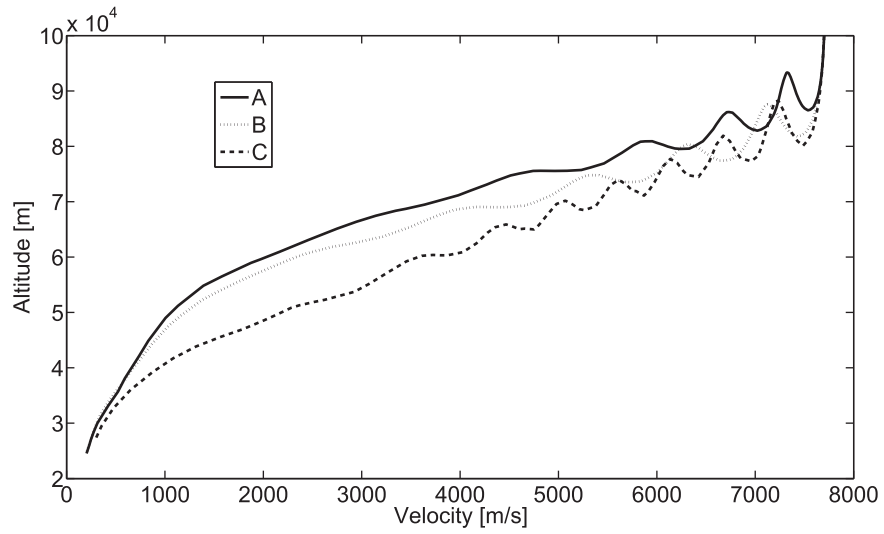
Fig. 6 Trajectories of the selected optimal solutions
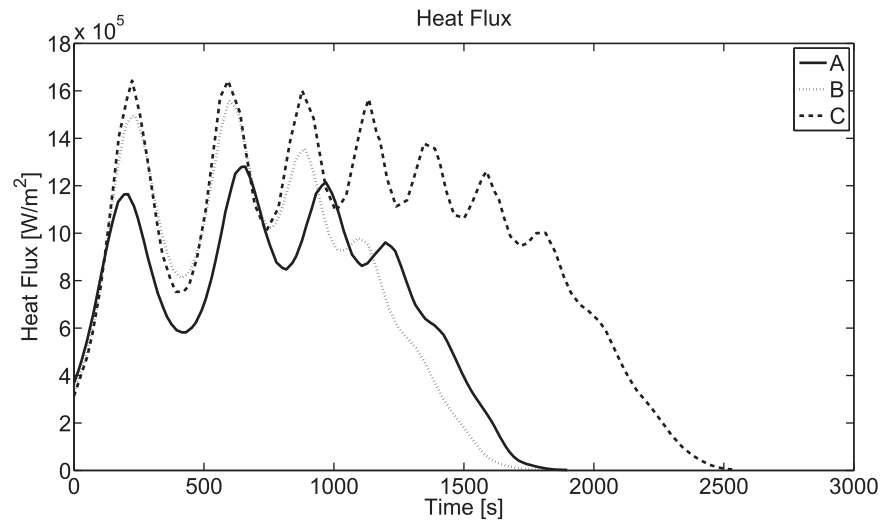
Fig. 7 Convective heat flux of the selected optimal solutions
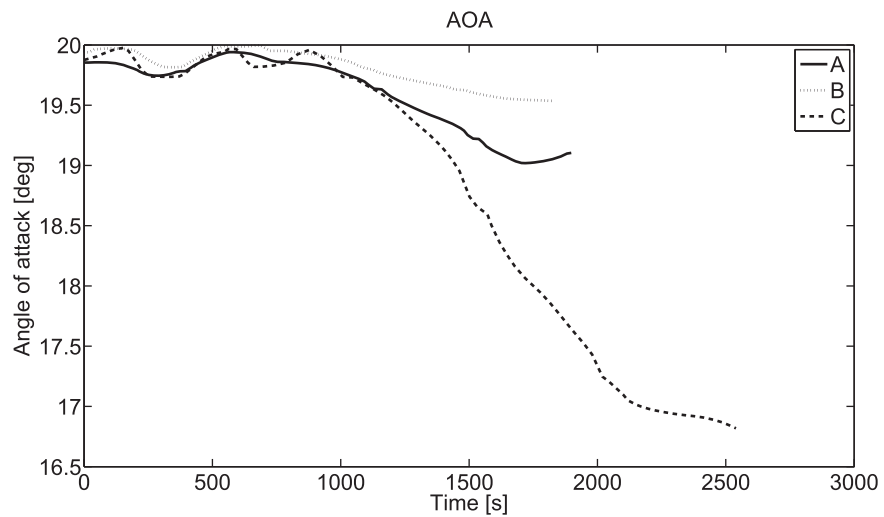
Fig. 8 Angle of attack control law
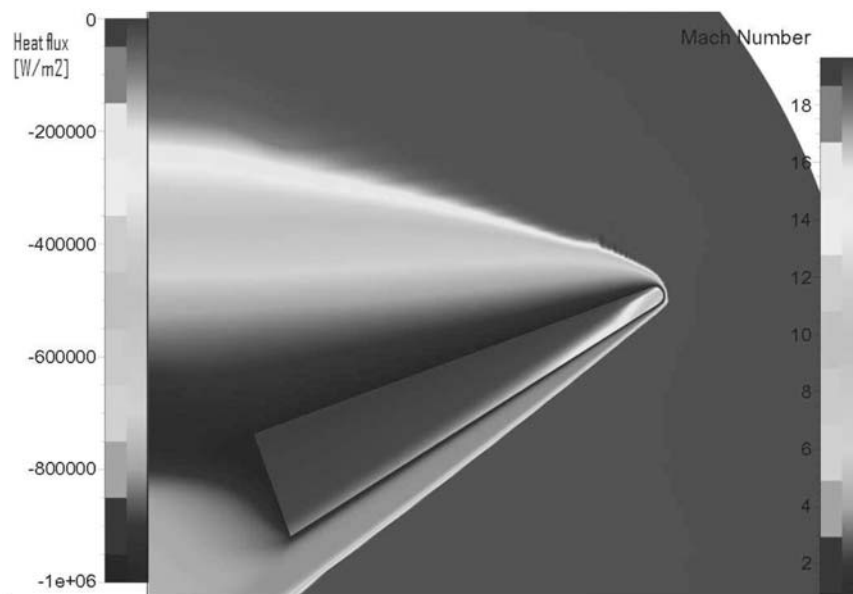
Fig. 9 CFD computation of individual A at conditions: $H = 75$ km, $v = 5500$ m/s, AoA $= 20°$. In the mirror plane, the Mach number contour, and on the vehicle the predicted heat flux contour are shown. As can be seen from the picture, the peak of the heat flux is still in the nose area

belly of the vehicle and the current model could not be applied.

5 CONCLUSIONS

This article addresses the robust design of a small-scale USV for re-entry operations. A procedure, which implements a combination of a global, population-based solver with a direct transcription method for optimal control problems, was proposed. The control problem solver is interfaced with an ANN system that gives the aerodynamic characteristics of the vehicle as a function of the geometric parameters and operational conditions. The ANNs are trained and upgraded by an evolution control procedure.

Uncertainties on the aerodynamic model and some characteristics of the thermal protection material are introduced into the vehicle model, and the evolutionary part of the code searches for shapes minimizing the mean value of the heat flux at the nose, the maximum internal temperature and the weighted sum of their variances.

The whole process was able to detect realistic optimal shapes, which will be the base for following studies on the design of such small space vehicles.

As expected, all the solutions do not have sharp edges and, as a consequence, they re-enter with an angle of attack which is towards the upper limit of $20°$. Since, in this study, the incidence is bounded to small values, the assumption that the maximum heating point is at the nose is still valid. On the other hand, for angles of attack of $40°$ or more, which is what it is

expected if the upper limit on the angel of attack is removed, the current model would need to be revised. In this latter case, a correct prediction of the real heating should be obtained by models of higher fidelity, which combines medium-to-high-fidelity aero-thermal dynamic computations. The authors are already working on this new modelling approach.

Further work is also required to correctly quantify the uncertainties. In particular, a numerical testing campaign will be needed to correlate the uncertainties with the fidelity of the models.

Moreover, since the internal control law is the result of a noisy min–max problem, current effort are already devoted to the quantification of the un-smoothness level of the process and to improve the convergence of the trajectory optimization, which strongly affects the performance of the obtained results. Future work will present the adopted methodology and its effect on the global, shape optimization process.

REFERENCES

1 **Umakant, J., Sudhakar, K., Mujumdar, P.,** and **Raghavendra Rao, C.** Ranking based uncertainty

quantification for a multifidelity design approach. *J. Aircraft*, 2007, **44**(2), 410–419.

2 **Doherty, J. J., Dean, S. R. H., Ellsmore, P.,** and **Eldridge, A.** A multi-fidelity approach for supporting early aircraft design decisions. In *Collaborative product and service life cycle management for a sustainable world* (Eds R. Curran, S. Y. Chou, A. Trappey), 2008, pp. 267–279 (Springer London, London).

3 **Choi, S., Alonso, J., Kroo, I.,** and **Wintzer, M.** Multifidelity design optimization of low-boom supersonic jets. *J. Aircraft*, 2008, **45**(1), 106–118.

4 **Choi, S., Alonso, J.,** and **Kroo, I.** Two-level multifidelity design optimization studies for supersonic jets. *J. Aircraft*, 2009, **46**(3), 776–790.

5 **Robinson, T., Eldred, M., Willcox, K.,** and **Haimes, R.** Surrogate-based optimization using multifidelity models with variable parameterization and corrected space mapping. *AIAA J.*, 2008, **46**(11), 2814–2822.

6 **Singh, G.** and **Grandhi, R.** Mixed-variable optimization strategy employing multifidelity simulation and surrogate models. *AIAA J.*, 2009, **48**(1), 215–223.

7 **Vasile, M.** and **Bernelli-Zazzera, F.** Optimizing low-thrust and gravity assist maneuvres to design interplanetary trajectories. *J. Astronaut. Sci.*, 2003, **51**(1), 13–35.

8 **Vasile, M.** and **Bernelli-Zazzera, F.** Targeting a heliocentric orbit combining lowthrust propulsion and gravity assist manoeuvres. In *Operational research in space & air*, first edition, vol. 79, 2003 (Kluwer Academy Press, Dordrecht, The Nederlands).

9 **Fornberg, B.** *A practical guide to pseudospectral methods*, 1998 (Cambridge University Press, Cambridge).

10 **Russo, G.** and **De Matteis, P. P.** Prora-usv: Two flight mission exploring transonic conditions. In Proceedings of the 15th AIAA International Space Planes and Hypersonic Systems and Technologies Conference, Dayton, Ohio, USA, 2008, AIAA 2008-2660. Proceedings published on CD-ROM.

11 **Savino, R., Paterna, D.,** and **Serpico, M.** Numerical and experimental investigation of prora usv subsonic and transonic aerodynamics. *J. Spacecraft Rockets*, 2006, **43**(3), 575–584.

12 **Russo, G.** Usv program status 2009. In Proceedings of the 16th AIAA/DLR/DGLR International Space Planes and Hypersonic Systems and Technologies Conference, Washington, DC, 2009, AIAA-2009-7269. Proceedings published on CD-ROM.

13 **Viviani, A.** and **Pezzella, G.** Heat transfer analysis for a winged reentry flight test bed. *Int. J. Eng.*, 2009, **3**(3), 330–345.

14 **Squire, T. H.** and **Marschall, J.** Material property requirements for analysis and design of UHTC components in hypersonic applications. *J. Eur. Ceram. Soc.*, 2010, **30**(1), 2239–2251.

15 **Strohmeyer, D., Eggers, T.,** and **Haupt, M.** Waverider aerodynamics and preliminary design for two-stage-to-orbit missions, part 1. *J. Spacecraft Rockets*, 1998, **35**(4), 450–458.

16 **Heinze, W.** and **Bardenhagen, A.** Waverider aerodynamics and preliminary design for two-stage-to-orbit missions, part 2. *J. Spacecraft Rockets*, 1998, **35**(4), 459–466.

17 **Starkey, R. P.** and **Lewis, M. J.** Analytical off-design lift-to-drag-ratio analysis for hypersonic waveriders. *J. Spacecraft Rockets*, 2000, **37**(5), 684–691.

18 **Chapman, C. J.** *High speed flow*, 2000 (Cambridge University Press, Cambridge).

19 **White, F. M.** *Viscous fluid flow*, 1974 (McGraw-Hill, New York).

20 **Aupoix, B.** and **Cousteix, J.** Real gas effects in two- and three-dimensional hypersonic, laminar boundary layers. In *Computational methods in hypersonic aerodynamics* (Ed. T. K. S. Murthy), 1991, pp. 293–340 (Kluwer Academic Publishers, Dordrecht, The Nederlands).

21 **Pezzella, G.** and **Viviani, A.** Aerodynamic analysis of a manned space vehicle for missions to mars. *J. Thermodyn.*, 2011, **2011**, 1–13.

22 **Savino, R., De Stefano Fumo, M., Paterna, D.,** and **Serpico, M.** Aerothermodynamic study of UHTC-based thermal protection systems. *Aerospace Sci. Technol.*, 2005, **9**, 151–160.

23 **Anderson, J. D.** *Hypersonic and high-temperature gas dynamics*, second edition, 2006, (AIAA, Virginia).

24 **Cowart, K.** and **Olds, J.** *Integrating aeroheating and TPS into conceptual RLV design*, 1999, AIAA 99-4806 (AIAA, New York, USA).

25 **Hankey, W. L.** *Re-entry aerodynamics (AIAA education series)*, 1988 (AIAA, New York, USA).

26 **Lozano, J. A., Larranaga, P.,** and **Inza, I.** *Towards a new evolutionary computation: advances on estimation of distribution algorithms (studies in fuzziness and soft computing)*, February 2006 (Springer, Berlin Heidelberg, Germany).

27 **Costa, M.** and **Minisci, E.** MOPED: a multi-objective parzen-based estimation of distribution algorithm. In *Evolutionary multi-criterion optimization. second international conference, EMO 2003* (Eds C. M. Fonseca, P. J. Fleming, E. Zitzler, K. Deb, L. Thiele), 8–11 April 2003, Vol. 2632 of *LNCS* pp. 282–294 (Springer, Faro, Portugal).

28 **Avanzini, G., Biamonti, D.,** and **Minisci, E. A.** Minimum-fuel/minimum-time maneuvers of formation flying satellites. In Proceedings of the Astrodynamics Specialist Conference, AAS 03-654, Big Sky, Montana, 3–7 August 2003.

29 **Deb, K., Pratap, A., Agarwal, S.,** and **Meyarivan, T.** A fast and elitist multiobjective genetic algorithm: NSGA-II. *IEEE Trans. Evol. Comput.*, 2002, **6**(2), 182–197.

30 **Fukunaga, K.** *Introduction to statistical pattern recognition*, 1972 (Academic Press, New York).

31 **Jin, Y., Olhofer, M.,** and **Sendhoff, B.** Framework for evolutionary optimization with approximate fitness functions. *IEEE Trans. Evol. Comput.*, 2002, **6**(5), 481–494.

32 **Forrester, A. I., Sobester, A.,** and **Keane, A. J.** *Engineering design via surrogate modelling: a practical guide*, 2006 (Wiley, Chichester, USA).

33 **Shyy, W., Papila, N., Vaidyanathan, R.,** and **Tucker, K.** Global design optimization for aerodynamics and

rocket propulsion components. *Prog. Aerospace Sci.*, 2001, **37**, 59–118.

34 Giannakoglou, K. C. Design of optimal aerodynamic shapes using stochastic optimization methods and computational intelligence. *Prog. Aerospace Sci.*, 2002, **38**, 43–76.

35 MacKay, D. J. C. Bayesian interpolation. *Neural Comput.*, 1992, **4**(3), 415–447.

APPENDIX 1

Notation

c	specific heat [J/kg · K]
C^*	Chapman–Rubensin parameter
C_D	drag coefficient
C_E	sampling hypersurface
C_L	lift coefficient
d	design vector
d_{boby}	thickness of the structure [m]
$d_{min,ll}$	minimum euclidean distance between the sampled trajectory point and the points of the database, evaluated with a lower fidelity code, to accept the new point into the database
$d_{min,sl}$	minimum euclidean distance between the sampled trajectory point and the points of the database evaluated with the same fidelity code, to accept the new point into the database
d_{sl}	euclidean distance between point in DB_{train} and the trajectory points extracted by the current solutions
d_{TPS}	thickness of the TPS skin covering the vehicle [m]
D	drag [N]
$\mathbf{DB}_{train}$	matrix of points in the database used to train the ANNs
D_v	viscous drag [N]
D_w	Wave drag [N]
E_q, E_T	mean values of the maximum heat flux and internal temperature, respectively
Err	error function
H	altitude [m]
k	thermal conductivity [W/m · K]
K_e	constant term in the heat flux equation (1.742 10^{-4})
l	nominal length of the waverider [m]
L	Lift [N]
L_{det}	Deterministic value of the Lift [N]
L_{TPS}	thickness of the TPS at the nose
L_{unc}	Value of the Lift affected by uncertainties [N]
m	total mass of the vehicle [kg]
m_{nose}	mass of the TPS at the nose [kg]
m_{skin}	mass of the TPS covering the vehicle [kg]
m_{st}, m_{TPS}, m_{pl}	structural mass, the mass of the TPS, and the mass of the payload (avionics and power system), respectively [kg]
Ma	Mach number
n	power law exponent for the shape of the waverider
n_k	number of kernels
n_{gcyc}	defines the generation loop in the generation-based evolution control approach
n_{gl}	number of generations of the global optimizer, for which the fidelity of the model is increased the upper level
n_{gv}	number of generations for which the real model has to be used for the generation-based evolution control approach
n_o	number of trajectory points to extract from each trajectory
n_p	number of collocation points
n_t	maximum number of trajectory point to extract for each generation
n_v	number of individuals to evaluate by true model in the individual-based evolution control approach
N	number of trajectory elements
P_u, P_b, P_b	pressure on upper, lower, and base surfaces, respectively [Pa]
$\dot{q}_{conv}$	convective heat flux [W/m²]
r	norm of the position vector with respect to the centre of the planet [m]
r_f	upper bound of the constraints on the final radius [m]
r_{min}	lower bound of the constraints on the final radius [m]
Re	Reynolds number
R_E	mean radius of the Earth (const. 6.371 10^6 m)
R_n	radius of curvature at the edges of the vehicle [m]
S	matrix with data of the trajectory
S_n	surface of the TPS nose cone [m²]
S_p, S_b	planform and base surface, respectively [m²]
S_{TPS}	TPS surface area except that of the nose [m²]
t	time [s]

T_e	temperature at edge of boundary layer in post-shock conditions [K]	θ	centre-line wedge angle of the waverider
T_{int}	internal temperature, measured at the end of the nose [K]	θ_p	flight path angle [degree]
v	magnitude of the velocity [m/s]	λ	longitude [degree]
v_e	flow velocity at edge of boundary layer in post-shock conditions [m/s]	ξ	heading angle (azimuth of the velocity) [degree]
V_n	volume of the nose [m^3]	ρ_{body}	density of the vehicle structure [kg/m^3]
V_∞	free stream velocity module [m/s]	ρ_e	air density at edge of boundary
w	nominal width of the waverider [m]		layer in post-shock conditions
x	longitudinal coordinate		[kg/m^3]
		ρ_{TPS}	density of the TPS material
α	angle of attack [degree]	σ	the Stephen–Boltzmann's constant
β	oblique shockwave inclination		(5.6704 10^{-8} W / m^2 K^4)
	angle of the waverider	σ_q^2, σ_T^2	variance of the maximum heat
γ_v	bank angle [degree]		flux and internal temperature, respectively
ϵ	material emissivity	ϕ	latitude [degree]